Journal of Structural Geology 91 (2016) 130–143

Contents lists available at ScienceDirect

Journal of Structural Geology

journal homepage: www.elsevier.com/locate/jsg

Smoothing and re-roughening processes: The geometric evolution of a single fault zone

Katherine A.H. Shervais [a, *], James D. Kirkpatrick [b]

[a] Department of Geoscience, Colorado State University, 1482 Campus Delivery, Fort Collins, CO 80524, USA
[b] Department of Earth and Planetary Sciences, 3450 University St., Montréal, QC H3A 0E8, Canada

ARTICLE INFO

Article history:
Received 11 February 2016
Received in revised form
2 September 2016
Accepted 5 September 2016
Available online 7 September 2016

Keywords:
Fault roughness
Fault core
Fault geometry evolution
Fault
Low angle normal fault
Principal slip zone

ABSTRACT

The geometry of a fault zone exerts a major control on earthquake rupture processes and source parameters. Observations previously compiled from multiple faults suggest that fault surface shape evolves with displacement, but the specific processes driving the evolution of fault geometry within a single fault zone are not well understood. Here, we characterize the deformation history and geometry of an extraordinarily well-exposed fault using maps of cross-sectional exposures constructed with the Structure from Motion photogrammetric method. The La Quinta Fault, located in southern California, experienced at least three phases of deformation. Multiple layers of ultracataclasite formed during the most recent phase. Crosscutting relations between the layers define the evolution of the structures and demonstrate that new layers formed successively during the deformation history. Wear processes such as grain plucking from one layer into a younger layer and truncation of asperities at layer edges indicate that the layers were slip zones and the contacts between them slip surfaces. Slip surfaces that were not reactivated or modified after they were abandoned exhibit self-affine geometry, preserving the fault roughness from different stages of faulting. Roughness varies little between surfaces, except the last slip zone to form in the fault, which is the smoothest. This layer contains a distinct mineral assemblage, indicating that the composition of the fault rock exerts a control on roughness. In contrast, the similar roughness of the older slip zones, which have comparable mineralogy but clearly crosscut one another, suggests that as the fault matured the roughness of the active slip surface stayed approximately constant. Wear processes affected these layers, so for roughness to stay constant the roughening and smoothing effects of fault slip must have been approximately balanced. These observations suggest fault surface evolution occurs by nucleation of new surfaces and wear by competing smoothing and re-roughening processes.

1. Introduction

The non-planar shape, or roughness, of fault surfaces exerts a fundamental control on fault strength and stability (Lay et al., 1982; Aki, 1984; Okubo and Dieterich, 1984; Power et al., 1988; Dieterich, 1992). Contact and mechanical interaction of geometric asperities across a fault surface impact earthquake nucleation, slip distribution, dynamic weakening processes, near-fault stress fields and source parameters such as moment release, radiated energy and stress drop (Chester and Chester, 2000; Brodsky and Kanamori, 2001; Parsons, 2008; Griffith et al., 2010; Dunham et al., 2011; Shi and Day, 2013). Measurements of exposed surfaces using digital profiling tools show that the asperities, or bumps, that define fault roughness range in size from micrometers to hundreds of meters and that roughness is self-affine (e.g. Renard et al., 2006; Sagy et al., 2007; Candela et al., 2012), meaning that asperity profiles change systematically as a function of scale.

Roughness measurements also show that surfaces of mature faults are smoother than immature faults and that all surfaces are smoother in the slip-parallel direction compared to the slip-perpendicular direction (Sagy et al., 2007; Candela et al., 2012). These observations imply that fault-surface geometry evolves with displacement towards smoother profiles, but compilations of roughness measurements from many faults suggest the smoothing occurs at a gradual rate (Sagy et al., 2007; Brodsky et al., 2011), perhaps due to inefficient wear processes (Power et al., 1987). One

* Corresponding author.
E-mail address: kshervais@gmail.com (K.A.H. Shervais).

http://dx.doi.org/10.1016/j.jsg.2016.09.004
0191-8141/

key missing constraint is the evolution of roughness over the deformation history of a single fault zone, which has never been measured.

Wear processes on a fault surface cause the geometry of the surface to change. Wear occurs via a variety of processes, such as abrasion, ploughing, grain plucking, grinding, and fracture exploitation (Engelder and Scholz, 1976; Doblas, 1998; Boneh et al., 2013, 2014). These processes create grooves on a fault surface, slice off asperities, and integrate new fracture surfaces into the main fault surface, which may all contribute to a change in its shape. They have previously been interpreted as transient rather than steady-state processes in nature due to the fractal nature of fault surfaces (Power et al., 1988).

Field data indicate that the smoothing of a fault surface is a function of displacement on the fault (Brodsky et al., 2011), suggesting wear processes occur continuously during slip. However, experimental work has shown that wear rates are dependent on normal stress (Wang and Scholz, 1994; Boneh et al., 2013; Lyakhovsky et al., 2014) and are also scale-dependent (Boneh et al., 2014; Davidesko et al., 2014). Spatially variable wear rates due to stress heterogeneity and the scale of displacement compared to a population of asperities may therefore result in a complex evolution of asperities on a fault surface (Dieterich and Linker, 1992; Linker and Dieterich, 1992). Elastic and inelastic deformation of the fault surface also causes scale-dependent wear, as asperities break at one scale but may glide past each other at another scale (Wang and Scholz, 1994; Kirkpatrick and Brodsky, 2014). Evidence for wear processes has rarely been observed in the field, where the size of exposure is comparable to the magnitude of coseismic displacement during a single earthquake (Sibson, 1986; Scholz, 1987; Wang and Scholz, 1994; Wilson et al., 2003). Furthermore, as no fault has ever been shown to be perfectly smooth, some additional processes contribute to the evolution of fault geometry, or limit the smoothing effect of the wear processes.

In this study, we take advantage of exceptional exposures of the La Quinta Fault in the Eastern Peninsular Ranges of southern California, which contains evidence for multiple generations of slip events. Because the fault is exposed in cross section rather than as a slickenside surface, we can use crosscutting relationships and mineral assemblages to interpret the deformation history of the fault and infer the relative ages of the multiple generations of slip surfaces. We measure the roughness of the edges of the slip surfaces over length scales from centimeters to ten meters and describe wear processes within the fault core. We use the results to assess the mechanisms that cause fault-surface geometry to change and the influence of fault rock composition, and evaluate how wear results from competition between smoothing and re-roughening processes.

2. Geologic setting

The La Quinta Fault crops out in Coyote Canyon in the Eastern Peninsular Ranges of southern California, one of the mountain ranges bounding the Coachella Valley (Fig. 1a) (Matti et al., 2006; previously referred to as the Coyote Creek fault by Wenk et al., 2000). The fault has an average orientation of 297/17°NE based on 14 measurements of fault slip surface orientations along strike. Dip-slip slickenlines have an average rake of ~80° from the east. Continuous over a mapped trace length of 9.4 km, the fault juxtaposes Asbestos Mountain tonalite in the hangingwall and Palm Canyon Metamorphic Complex in the footwall (Sharp, 1979). The Asbestos Mountain batholith varies in composition, but is generally described as a biotite-hornblende rich tonalite containing a weak regional foliation (Morton et al., 2014). The Palm Canyon Metamorphic Complex is a deformed metasedimentary complex composed of a variety of gneisses as well as migmatites, pelitic schists, amphibolites, pyroxenties, and marbles (Sharp, 1967; Morton et al., 2014). The Asbestos Mountain tonalite intrudes the Palm Canyon complex away from the fault contact. Our study focuses on exposures in Coyote Canyon and the area east of the mouth of Deep Canyon (Fig. 1b). The extent of the fault to the north of the study area, and beyond the Martinez Mountain landslide to the south is unknown, but is thought to continue for ~30 km (Fig. 1a) (Matti et al., 2006).

The fault is parallel to the nearby Santa Rosa Mylonite Zone (SRMZ), which crops out ~9 km to the west of the La Quinta Fault trace (Fig. 1a) (Goodwin and Renne, 1991). The hangingwall of the SRMZ also contains the Asbestos Mountain tonalite. Thermal histories derived from fission track, $^{40}Ar/^{39}Ar$, K/Ar, and U/Pb ages for the Asbestos Mountain tonalite and the Palm Canyon Complex adjacent to the SRMZ suggest cooling was rapid and that both reached a temperature of <300 °C ca. 70 Ma, likely constraining the earliest time of activity for the La Quinta Fault (Armstrong and Suppe, 1973; Dokka, 1984; Goodwin and Renne, 1991; Wenk et al., 2000). This interpretation is supported by $^{40}Ar/^{39}Ar$ dating of pseudotachylytes, which cut Asbestos Mountain tonalite and Palm Canyon Complex in Coyote Canyon and north of the Martinez Mountain landslide. They indicate brittle faulting during the Laramide at ~56–62 Ma as well as potential periods of activity around ~74 Ma and 40 Ma (Wenk et al., 2000).

Field evidence indicates a post-Laramide phase of deformation on the La Quinta Fault, but few direct timing constraints are available for confirming the timing of one or more slip events. Multiple parallel faults dipping shallowly toward the east-northeast of a similar or larger size than the La Quinta Fault exist in the region, including the West Salton Detachment Fault ~25 km to the south, which are interpreted as Laramide-era thrusts reactivated as extensional detachment structures in the Miocene (Axen and Fletcher, 1998). Post-Laramide deformation of the La Quinta Fault may also have involved normal reactivation of a pre-existing thrust fault (Sharp, 1979; Erskine, 1985, 1986; Todd et al., 1988). However, basal conglomerates on fault dip-slopes and piercing points that were used to delimit Miocene extension are not present for the La Quinta Fault in Coyote Canyon (Dorsey et al., 2011; Janecke et al., 2010), possibly because of rapid uplift in the Santa Rosa Mountains or erosion along the fault trace.

In addition to this potentially complex deformation history, we have not found any piercing points to measure the net displacement across the La Quinta Fault, or the displacement associated with any of the phases of deformation described below. Based on scaling relationships, a trace length of 10–30 km suggests a total displacement of the order of hundreds of meters or more (e.g. Cowie and Scholz, 1992).

3. Field and microstructural observations of the La Quinta Fault

The La Quinta Fault is extraordinarily well exposed due to erosion at the base of Coyote Canyon (Figs. S1–S5 in Supplementary Material). The fault has a distinctive architecture consisting of an ultracataclasite-filled inner fault core, an outer fault core that is crosscut by the inner fault core, and an extensive damage zone (Rowe et al., 2012). The inner and outer fault cores have a combined thickness of 12–17 m, varying along strike due to thickness variations for both. The total fault width is ~75 m due to the extent of the flanking damage zone. The outer fault core contains cataclasites crosscut by subsidiary faults that splay from the inner fault core. Multiple layers of crosscutting, discontinuous ultracataclasite define the inner fault core. The number of distinct ultracataclasite layers within the inner fault core varies from one to 12 along strike.

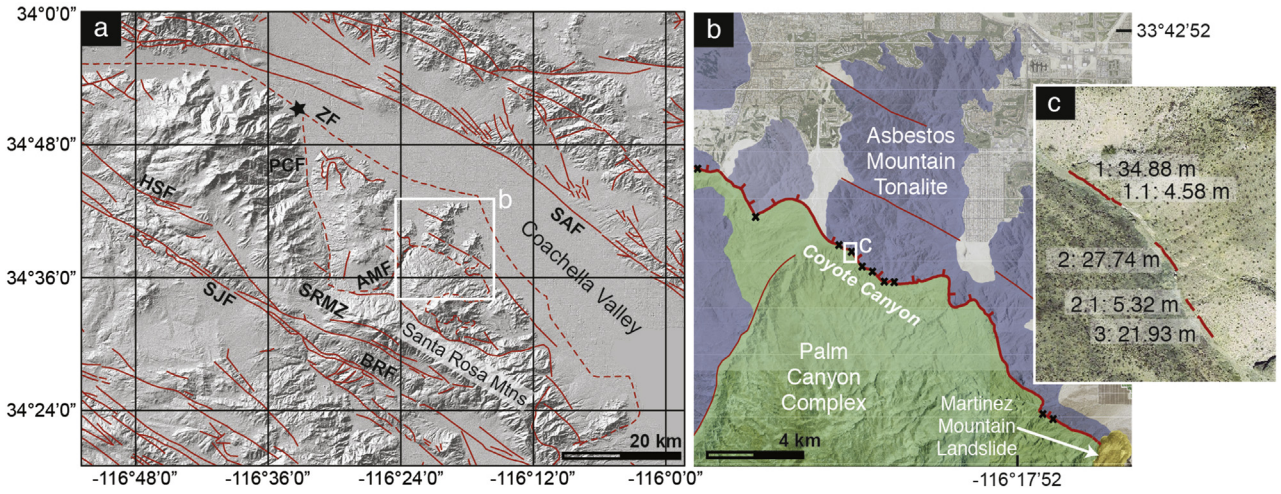

Fig. 1. Location map: a: Regional map of topography and major fault strands (red) in the vicinity of the La Quinta Fault (faults from Ludington et al., 2005). Dashed lines indicate faults that were active as low-angle structures (from Janecke et al., 2010; Matti et al., 1983). The city of Palm Springs is shown by the star. AMF: Asbestos Mountain Fault; BRF: Buck Ridge Fault; HSF: Hot Springs Fault; PCF: Palm Canyon Fault; SAF: San Andreas Fault; SJF: San Jacinto Fault; SRMZ: Santa Rosa Mylonite Zone; and ZF: Zosel Fault. b: Map showing the location of the La Quinta Fault in the Eastern Peninsular Ranges of southern California (fault is the thick red line; solid where location is known and dashed where inferred. Other faults from Ludington et al. (2005) shown by thin red lines). Crosses show locations where the characteristic internal geometry defined by the presence of layer m is exposed. Geology modified from Sharp (1979), Wenk et al. (2000), White (2006), and Matti et al. (2006). c: Locations of the five exposures used for during this study. Total length from exposure 1 to exposure 3 is 167 m. (For interpretation of the references to colour in this figure legend, the reader is referred to the web version of this article.)

All ultracataclasite layers truncate other layers, indicating that each was a slip zone at some stage during the deformation history. One continuous ultracataclasite layer within the inner fault core, referred to here as layer m, crosscuts all other deformation structures, and is interpreted as the youngest slip zone on the fault.

3.1. Methods

The five extensive exposures of the La Quinta Fault selected for this study provided a high percentage of exposed fault (56.5%) relative to covered areas (43.5%) over a 167 m distance along strike (Fig. 1, Figs. S1–S5). These exposures are located at the base of cliffs in the riverbed of Coyote Canyon, which trends ~305°, approximately parallel the strike of the fault. The exposure lengths are 34.9 m, 4.58 m, 27.7 m, 5.31 m and 21.9 m, and the trend of each is 17° or less off the strike direction.

We mapped the internal structure of the fault using high-resolution rectified images produced with the Structure from Motion (SfM) methodology. SfM uses traditional stereophotogrammetry techniques to build a 3D model with integrated color of objects or scenes from photographs with large variations in location and view direction (Johnson et al., 2014). After removing large debris and dirt covering the inner fault core, exposures were brushed with a fine brush to remove dust, small pebbles, and organic material. The exposures were then extensively photographed, with an average of 5 photographs per meter, and input into Agisoft's Photoscan Pro software (Fig. 2a,b). The program generated a 3D model with overlain texture (color) maps of each exposure by matching pairs of points in the images (see Supplementary Material for example model, Fig. S1) (Verhoeven, 2011; Johnson et al., 2014). High resolution (1.2 mm/pixel) orthorectified images of each exposure were created by rotating the models to view the exposures looking down the displacement vector defined by slickenlines on exposed edges of the inner fault core and internal layers, i.e. in the direction of maximum roughness. The true thickness and geometry of the layers is apparent in the resulting cross sections through the fault.

The internal structure of the fault was mapped on an iPad in the field at each exposure. These maps were used to quantify the geometry and interpret the deformation history of the La Quinta Fault (Fig. 2c) (Supplementary Material, Figs. S2–S5). The traces of contacts between the inner and outer fault core, as well as all identifiable layers within the inner fault core were mapped. The contacts between the inner and outer fault core were defined by texture, grain size and composition differences. Layers within the inner fault core were mapped based on grain size, color, cohesion, fracture characteristics, clast composition, and clast abundance (similar to Chester and Chester, 1998). Real-time kinematic (RTK) differential GPS ground control points (accurate to 1 mm horizontally and 2 mm vertically) at the ends of each exposure were used to scale the traces to true exposure length, providing a physical dimension for subsequent observations of fault core geometry.

Damage-zone structural orientations and kinematics were recorded within 1–2 m of the outer fault core in the footwall and at locations 11 m, 60 m, and 120 m above the fault in the hangingwall. Samples of the extremely friable ultracataclasites were collected by applying low-viscosity resin to the exposures and carefully separating intact hand-sample-sized blocks. Lenticular clasts within the inner fault core were individually photographed, and their locations, dimensions, and compositions recorded. Clasts of all sizes in the ultracataclasite layers were mapped from SEM images, photomicrographs, and field photographs. The SEM images and photomicrographs were converted to binary images, and major and minor axis dimensions of clasts found using the 'Analyze Particles' function in the ImageJ image analysis software (Rasband, 1997). Clasts from field photographs were mapped by hand in Adobe Illustrator, converted to binary, and analyzed using the same function.

3.2. Fault zone architecture

The hangingwall outer fault core is up to ~2 m thick and is composed of Asbestos Mountain tonalite that contains a solid-state foliation that is locally cut by cataclasites, dikes, shear fractures, and remnant pseudotachylyte veins. The foliation, defined by aligned biotite and hornblende, is observed throughout the Asbestos Mountain batholith (Morton et al., 2014). The foliation orientation

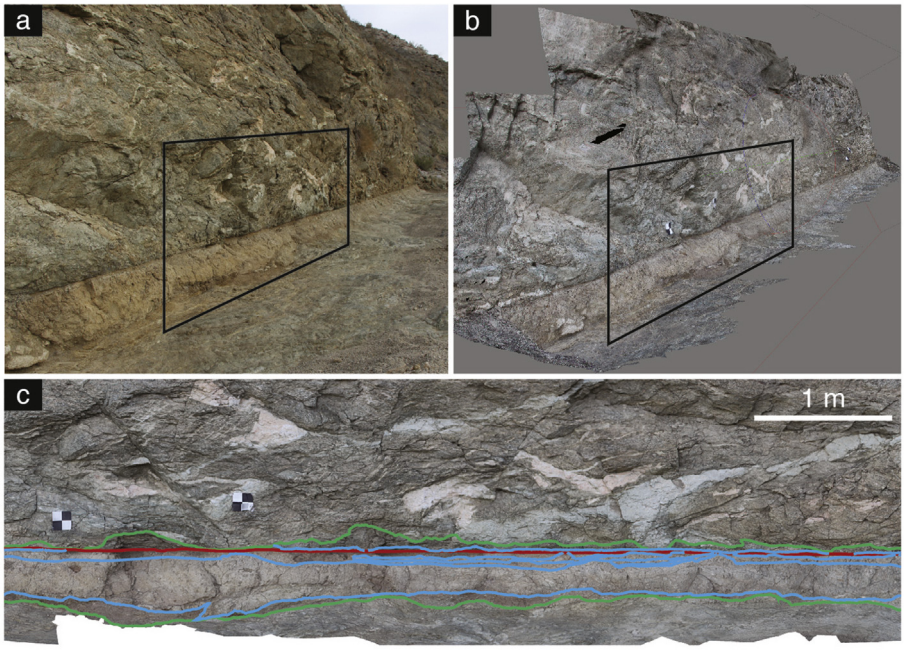

Fig. 2. Outcrop to field map workflow: a: Oblique photograph of Exposure 3. Around 150 photos similar to this one were used to construct the outcrop model. b: Model generated with Agisoft's PhotoscanPro shown from the same perspective as a. Boxes in a and b show the extent of c. c: Orthorectified photograph exported after the model was rotated to view the exposure in the orientation down the slip vector. Lines show traces mapped in the field that were used to calculate roughness. Red lines are layer m, green lines define the extent of the inner fault core, and blue lines show layers within the inner fault core. (For interpretation of the references to colour in this figure legend, the reader is referred to the web version of this article.)

varies widely along strike and increases in degree of deformation with proximity to the La Quinta Fault. Where oriented at an angle to the fault, it is truncated by ultracataclasite layers of the inner fault core. Dikes and pseudotachylyte veins both cut and exploit the foliation. Pseudotachylytes are present within the hangingwall outer fault core near the fault (within 2 m) and in the damage zone (observed up to 60 m above the fault). Pseudotachylye veins display quenched margins, flow banding, and complex fault- and injection-vein, and breccia geometries. They are mostly crosscut by damage-zone shear fractures, and are resultantly discontinuous along strike (Fig. 3). Survivor clasts are predominantly composed of quartz and feldspar, some of which display embayed margins, and are present in a matrix that contains compositional flow banding. Pseudotachylyte fault veins have an average orientation of 200/39°W (Fig. 3c). Cataclasite layers commonly completely overprint the foliation and host-rock phaneritic texture. At microscopic scale, the hangingwall outer fault-core cataclasite is composed of shattered clasts of quartz and seriticized plagioclase with intact chlorite grains (see Fig. 4). Cataclasite, foliation, dikes, and pseudotachylytes are all crosscut by numerous high-angle shear fractures that exhibit normal separation. Shear fractures in the hangingwall outer fault-core have a wide range of attitudes (Fig. 3d), but shear fractures in the damage zone generally dip steeply and strike approximately northwest (Fig. 3e).

The footwall outer fault core is defined by the presence of cataclastically deformed Palm Canyon Complex rocks cut by minor faults. The region with minor faults is approximately 10–15 m wide and is bound at its base by a subsidiary fault sub-parallel to the La Quinta Fault in the main study area. Individual fault-bounded blocks in the footwall outer fault core vary in mineral composition, degree of deformation, degree of development of foliation, and color (blueish to brownish green), but extensive quartz cementation means that all are cohesive fault rocks. Microscopically, outer fault core cataclasite is similar to the hangingwall outer fault core cataclasite with large (max. 4 mm) shattered clasts contained within an aphanitic matrix. Pseudotachylytes in the footwall outer fault core are aphanitic, appearing at the edge of and cross-cutting bands of cataclasite. Pseudotachylyte veins in this location are overprinted by shear fractures and the inner fault core.

The inner fault core consists of multiple layers of ultracataclasite, where each has a distinctive combination of clast content and composition, average grain size, and overall color (Fig. 3a). The inner fault core varies in total thickness from 8 to 75 cm, depending on the number of layers present, with an average thickness of 22 cm. Individual layers vary in thickness from one millimeter to over 40 cm, partially due to truncation by later slip events. Layers are pale tan to dark brown, with shades of orange and red. Matrix grains within all layers ranges from clay-sized to sand-sized. Clast content within the layers ranges from <10% to ~60%. Some layers contain orthogonal fractures spaced millimeters apart that terminate at layer edges that cause the ultracataclasite to break into small (sub cm) blocks.

These characteristics were used to identify thirteen distinct ultracataclasite layers in the field. These layers are referred to here as layers a to m. Layers are named alphabetically in order of interpreted formation, such that a is the oldest layer and m is the youngest. The layers are discontinuous along strike, and only one (layer m) is continuous throughout the study area, but crosscutting relationships allowed a relative chronology to be developed (see Supplementary Material for details of relative layer chronology). Layers were interpreted as older where truncated by other layers, offset by shear fractures, present as clasts within other layers, or some combination of these characteristics. Generally, older layers have a larger grain size, larger clasts, and also tend to have less dense fracture networks or none at all, and consequently, these layers are more cohesive. Relatively younger layers have a very fine grain size with smaller and less common clasts.

Clasts are present in every layer with sizes from sub-micron to

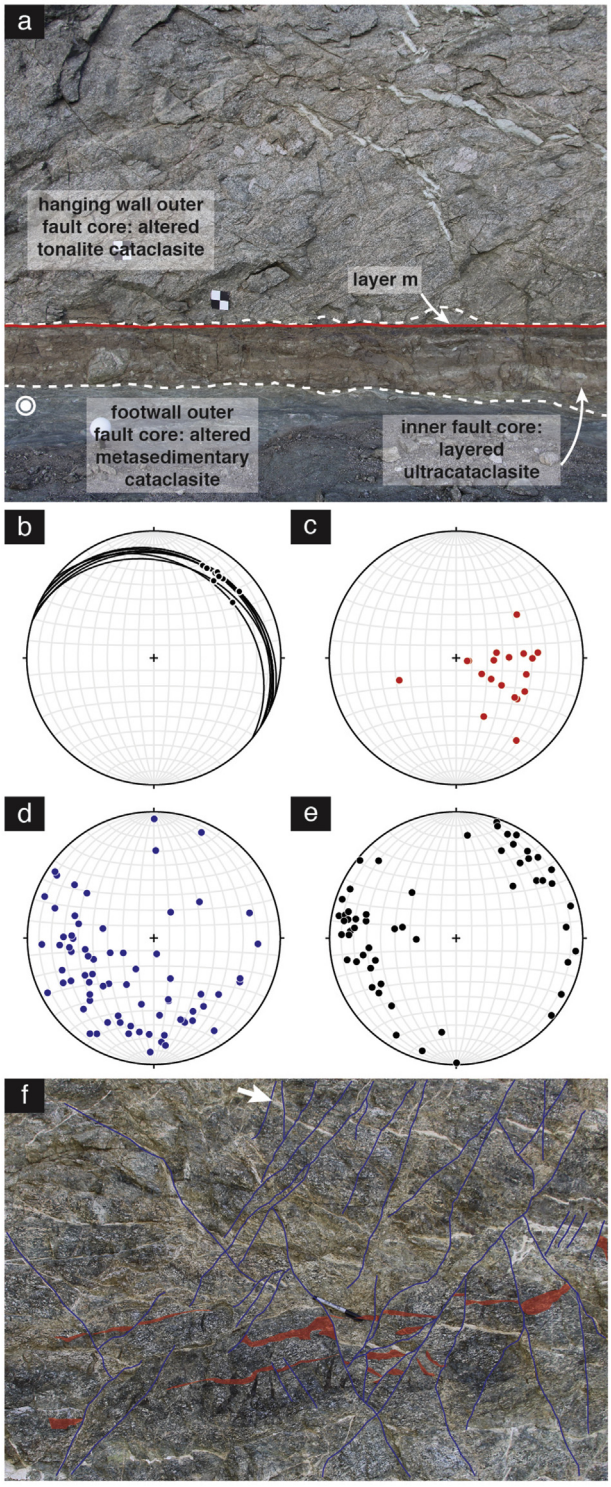

Fig. 3. Architecture of the La Quinta Fault: a: photograph illustrating the internal architecture of the La Quinta Fault. View is approximately in the down-dip direction to the NNE. Layer m is identified with the red line, the dashed white lines show the boundaries of the inner fault core, and the bull's-eye shows the slip sense in the viewing direction. b: fault orientation data measured at 14 locations along strike including the trend and plunge of slickenlines on exposed fault surfaces. c: Poles to pseudotachylyte fault veins in the hangingwall damage zone. d: Poles to shear fractures within the hangingwall outer fault core. e: Poles to shear fractures in the hangingwall damage zone. f: Photograph showing hangingwall outer fault-core shear fractures (blue) with normal-sense apparent offsets. White arrow indicates a thin dyke that is offset and example pseudotachylyte fault veins that are offset are shown in red. View to the SE, approximately orthogonal to dip on the La Quinta Fault. (For interpretation of the references to colour in this figure legend, the reader is referred to the web version of this article.)

tens of centimeters and have a wide range of aspect ratios (Fig. 5). Clasts range from equidimensional to lenticular in shape and are composed of reworked inner fault-core ultracataclasites, with some clasts from layers that are apparently no longer present, as well as outer fault-core cataclasite and tonalite (Fig. 5). Smaller clasts are more equidimensional whereas larger clasts have a wider range of aspect ratios (Fig. 5c). Lenticular clasts with an aspect ratio significantly <1 generally have a semi-elliptical shape, with one flat and one curved side. They range in size from 4 cm to a maximum of 34 cm long for tonalitic cataclasite, and 3–90 cm long for metasedimentary cataclasite. The orientations of the flat edges of these lenses vary. Both tonalitic and metasedimentary cataclasite lenses are observed with the flat edge of the clast facing toward their protolith as well as facing away from their protolith. The thickness of a given lenticular clast is typically similar to the thickness of the host ultracataclasite layer.

In general, the inner fault core crosscuts structures in the outer fault core but the arrangement of the fault elements has complexities. For example, in one exposure the outer fault core locally truncates layers of inner fault core (Fig. 6a). At another location, only two ultracataclasite layers are continuous, including layer m, representing a thin region of the inner fault core (see Supplementary Material). Additionally, the inner fault core is disrupted where conjugate subsidiary fractures in the hangingwall outer fault-core cut and displace the contact between the inner and outer fault core. The thickness of the inner fault-core ultracataclasite layer adjacent to the outer fault core is either significantly increased or decreased where this geometry occurs depending on the subsidiary fracture orientation. The resultant modifications to the inner fault core affected only one layer, at a time, implying the layers deformed to fill the space created by synkinematic displacement on subsidiary fractures (Fig. 6b, c).

In addition to the crosscutting relationships, petrographic and XRD analyses show that the inner and outer fault cores are mineralogically distinct (methods and semi-quantitative analysis results in Supplementary Material Section 2 and Table S1). Samples analyzed by XRD illustrate the range of lithologies for the hangingwall and footwall outer fault cores, as well as variations in the degree of alteration. The hangingwall outer fault core is deformed and altered tonalite that contains quartz, albite, prehnite, laumontite, chlorite ± kaolinite ± anorthite ± epidote ± actinolite. The footwall outer fault-core composition is more variable, which we interpret to reflect the greater lithologic variation of the Palm Canyon complex, containing quartz, albite, anorthite, illite, epidote, ±chlorite, ±zeolite (laumontite or phillipsite) ± montmorillonite ± cristobalite ± calcite. This mineralogy represents a mixture of the pre-faulting amphibolite-facies metamorphic assemblage (quartz, anorthite), alteration products (zeolites, illite, epidote, chlorite, kaolinite, montmorillonite) and hydrothermal veins probably formed during alteration (cristobalite, calcite). The inner fault core contains quartz, albite, anorthite, laumontite, chlorite, epidote ± kaolinite. In addition, layer m contains a substantial amount of amorphous material, and the XRD spectrum for this sample shows a broad peak at ~13 Å, consistent with the presence of a smectite group clay, such as montmorillonite. No clay separates were prepared, so we cannot identify this clay with certainty or quantify its abundance.

3.3. Layer m

Layer m is a distinct ultracataclasite layer that crosscuts all other layers of the inner fault core and, in some places, the inner-outer fault-core contacts (Fig. 7). This layer is present in every exposure of the fault, unlike the other layers of ultracataclasite, and is always located adjacent to either the upper or lower edge of the inner fault

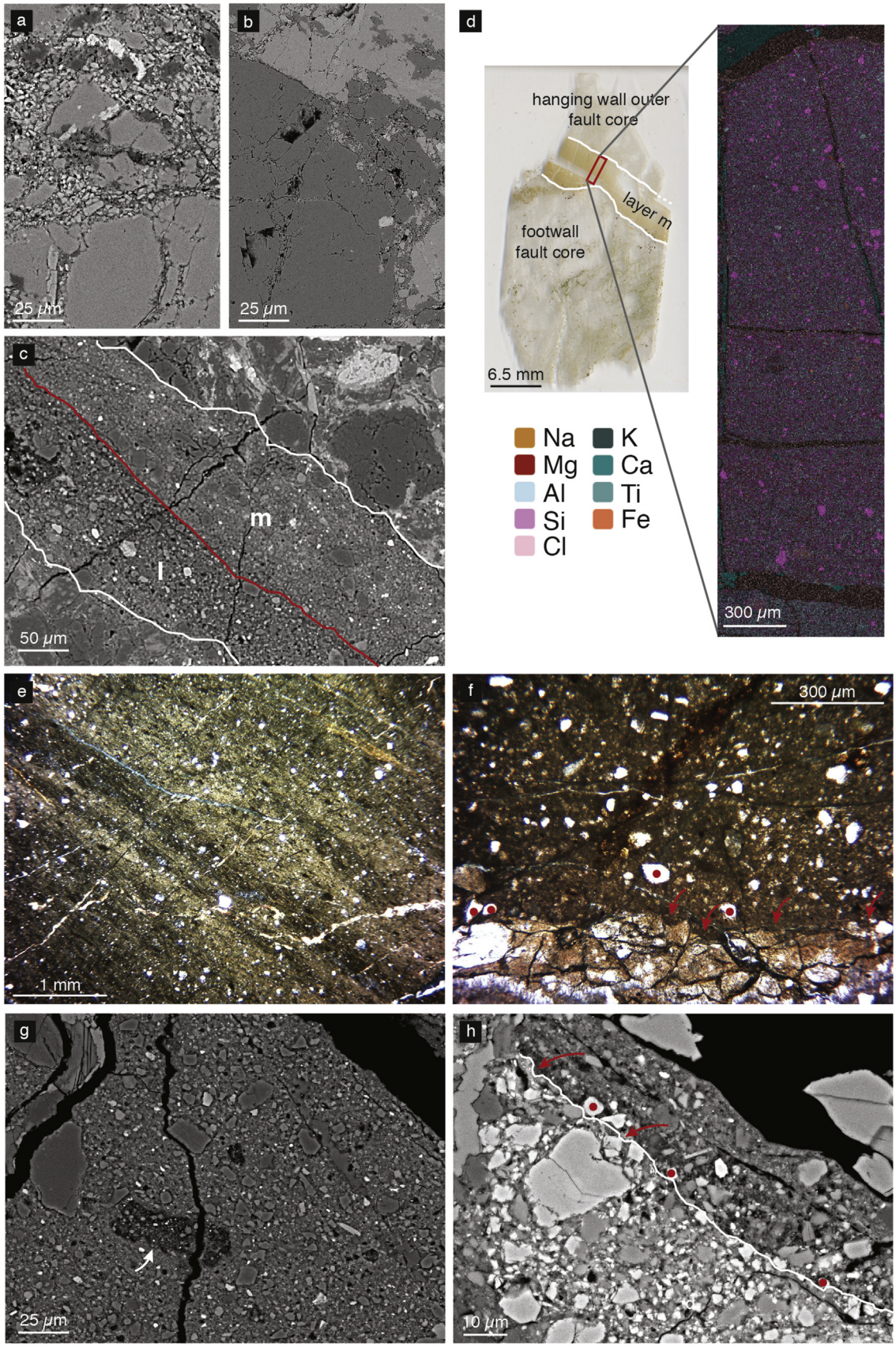

Fig. 4. Microstructure of the ultracataclasite layers. a: Scanning electron microscope back scattered electron (BSE) image of the hangingwall outer fault core. Note abundant, relatively large, angular to sub-angular clasts. b: BSE image at the same scale as a of the footwall outer fault core. Note the large clast size. c: BSE image of layer l and layer m in contact with the outer fault core; the contact between the two ultracataclasite layers is marked with a red line. Layer l (labeled) has a larger grain size than layer m, but both are

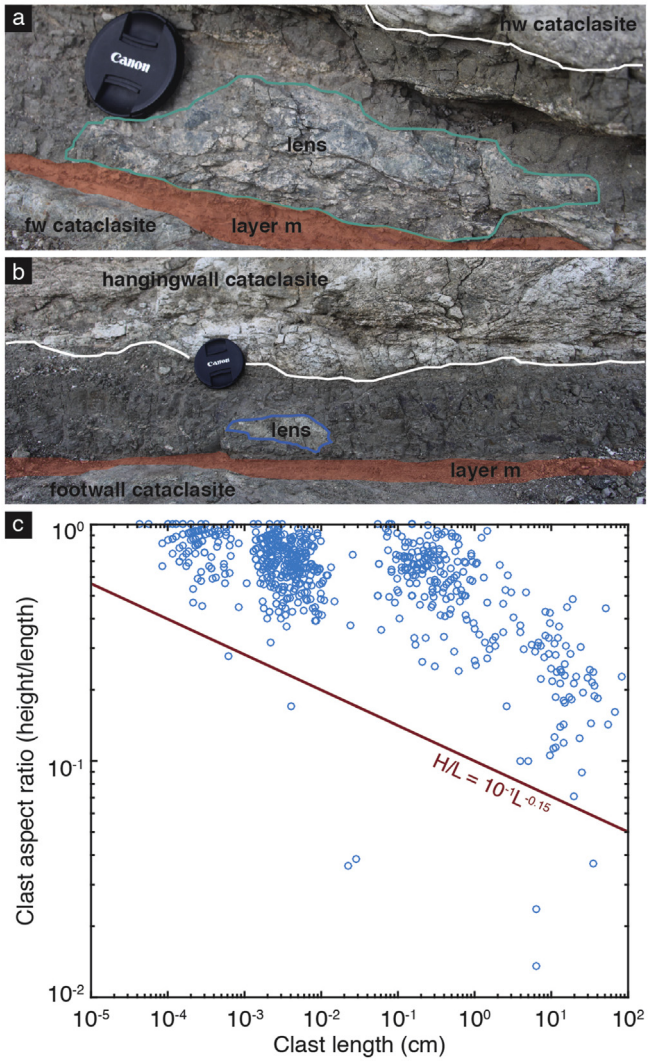

Fig. 5. Lenticular clasts in the inner fault core. a: Photograph showing an example of a lenticular clast from footwall outer fault-core material in the inner fault core. b: An example from the hangingwall outer fault core in the inner fault core. c: Clast aspect ratios plotted against clast maximum length for clasts from SEM images, photomicrographs, field photographs, and field measurements.

core. It is the finest grained of any of the fault rocks, has a homogeneous composition, and varies in thickness from 0.1 to 8 cm. The edges of the layer are planar in exposure, except for rare cases where the layer splays around lenses of other fault rock, leading to a local increase in thickness and a local undulation of the surface (Fig. 7b). Ultracataclasite injection veins branch from layer m into the hangingwall outer fault core (Fig. 7c). The injections typically have apertures comparable to the local thickness of layer m, and ultracataclasite from the entire thickness of layer m is continuous with the ultracataclasite in the injections.

Layer m is composed of sub-rounded to rounded clasts (~0.05–0.1 mm diameter) in an aphanitic matrix (Fig. 4). Thin section observations in cross-polarized light show the matrix commonly displays a foliation defined by spaced phyllosilicate grains aligned parallel to the layer edges. In places, 1–4 mm thick bands where the entire matrix contains aligned phyllosilicates are present. However, the edges of these bands do not truncate clasts within the layer, evidence for crosscutting relationships between the bands is lacking. Energy dispersive spectroscopy (EDS) maps show the chemical composition is consistent across layer m (Fig. 4d).

Clasts of quartz and plagioclase feldspar with rare clasts of chlorite and previously formed ultracataclasite make up ~20% of layer m (Fig. 4c). Optically visible clasts have an aspect ratio of ~0.4–1 (n = 100). At higher magnifications, smaller clasts, as well as the grains composing the matrix, can be distinguished as being angular to sub-angular, and show evidence of sub-micron scale fracturing (Fig. 4b, f). They have a slightly more limited range of aspect ratios (0.6–1) than the optically visible clasts. Clasts composed of the older layers of ultracataclasite and pseudotachylyte are occasionally present within layer m. The contact between layer m and the inner-outer fault core is generally planar at the grain scale, but includes local embayments where grains were plucked from the outer fault core (Fig. 4e, f).

4. Deformation history of the La Quinta Fault

Crosscutting relationships and compositional differences define the deformation history of the La Quinta Fault, though few direct timing constraints are available. At least three phases of deformation are evident: early ductile deformation, brittle formation of the outer fault core, and localization of brittle deformation into the inner fault core.

Both the Asbestos Mountain tonalite and Palm Canyon Complex contain foliations and folds that record ductile deformation. Foliation in the footwall outer fault core Palm Canyon Complex has been entirely overprinted by brittle deformation and hydrothermal mineralization up to 15 m from the fault. In contrast, hangingwall outer fault-core foliation, defined by aligned hornblendes and biotites, is gently folded at the exposure scale. The increase in degree of development of the regionally expressed foliation (Morton et al., 2014) toward the fault suggests foliation deflection as a result of an increase in strain during an early stage of the fault evolution. Thermochronologic data suggest the ductile deformation occurred from 87 Ma (emplacement of the Asbestos Mountain tonalite) to ~70 Ma when both the hangingwall and footwall cooled through 300 °C (Wenk et al., 2000).

Cataclastically deformed Asbestos Mountain tonalite and Palm Canyon Complex, as well as pseudotachylytes in the outer fault core crosscut the ductile structures showing brittle deformation postdated ductile deformation. The footwall outer fault core has a predominantly cataclastic texture varying in composition along strike as a result of variation in protolith lithology and subsidiary faulting. Pseudotachylyte veins in the footwall outer fault core appear between and within bands of cataclasite, indicating a synchronous formation. $^{40}Ar/^{39}Ar$ ages of pseudotachylytes sampled close to the La Quinta Fault are ~40 Ma, 56–60 Ma and ~73 Ma (Wenk et al., 2000). If the pseudotachylytes that we identified are comparable to those dated previously, the reported ages indicate

composed of ultracataclasite. d: EDS transect across layer m from the hangingwall outer fault core to the footwall outer fault core. The legend shows the elements present and their corresponding colors. No significant major or minor elemental variations are evident across the layer. e: Representative photomicrograph (cross polarized light) showing bands of aligned clay grains in the matrix of layer m (brighter regions). f: Thin section photomicrograph (plane polarized light) showing the contact between layer m (top) and the outer fault core (bottom). The contact is embayed (red arrows), which is interpreted to result from grains being plucked from the edge of the layer during shear across layer m (likely plucked grains indicated by red dots). g: BSE image at the same scale as a and b showing the matrix of layer m, which contains smaller, more rounded clasts than the outer fault core. The rectangular clast within the layer is composed of ultracataclasite (white arrow). h: BSE image of the same contact as in e. showing similar embayed contact and plucked grains (red arrow and red dots respectively). (For interpretation of the references to colour in this figure legend, the reader is referred to the web version of this article.)

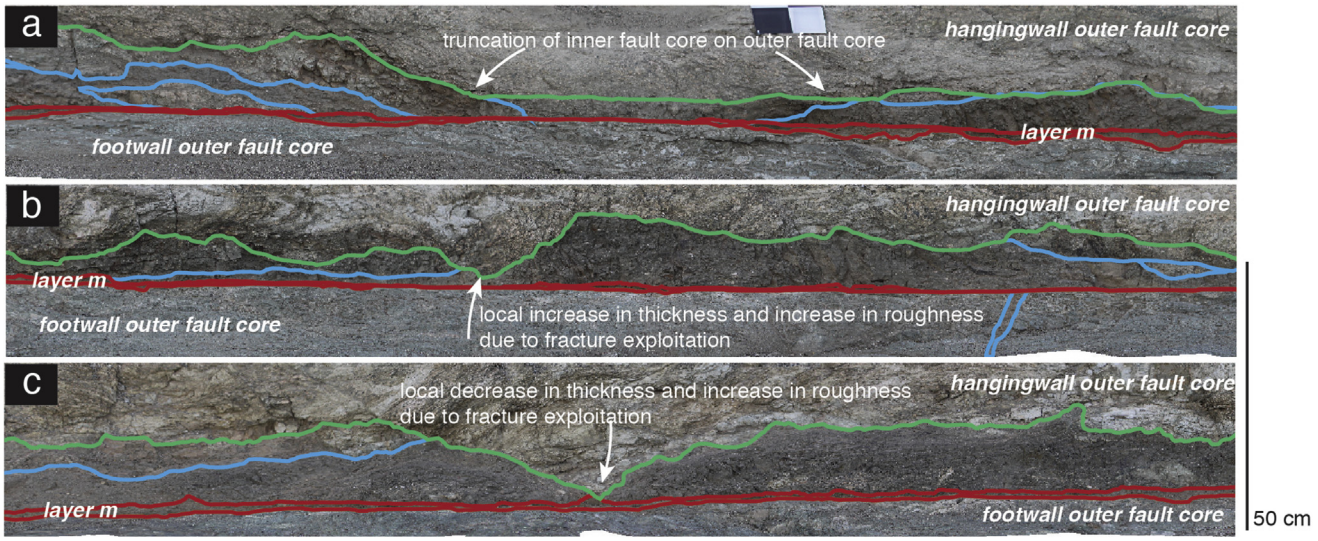

Fig. 6. Field observations of the inner fault core. Green lines are inner-outer fault core contacts, blue lines are ultracataclasite inner fault-core layers, and red lines are layer m. a: layers of ultracataclasite are truncated by hangingwall outer fault-core material, while layer m is continuous across the base of the fault core. b and c: the fault core increases locally in thickness due to the exploitation of fractures in the outer fault core. (For interpretation of the references to colour in this figure legend, the reader is referred to the web version of this article.)

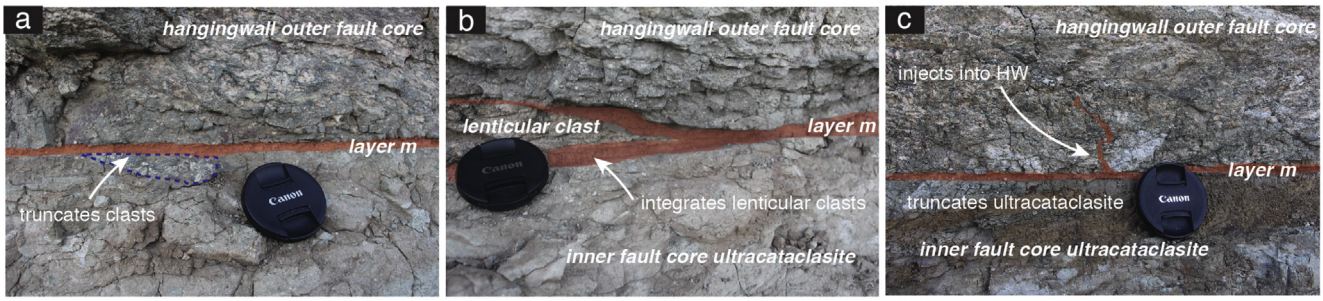

Fig. 7. Characteristics of layer m. a: Layer m (in red) truncates a large clast within an adjacent inner fault-core layer (camera lens for scale ~6 cm diameter). b: Layer m splays into the hangingwall outer fault core to integrate a lenticular clast of outer fault core material, locally increasing its thickness. c: An injection vein that branched from layer m into the hangingwall. Note layer m also crosscuts adjacent layer within the inner fault core (below the red layer). (For interpretation of the references to colour in this figure legend, the reader is referred to the web version of this article.)

Laramide-aged brittle deformation in the outer fault core.

Mineral assemblages in the hangingwall and footwall outer fault cores both contain relict phases associated with peak metamorphic grade, evidence for alteration at lower greenschist facies conditions, and also alteration at a lower metamorphic grade. For example, in the footwall outer fault core, albite, epidote, and chlorite are consistent with alteration at greenschist conditions, with zeolites, illite, kaolinite and montmorillonite representing a lower grade alteration assemblage. Two plagioclase compositions occur in both the footwall and hangingwall outer fault cores. Anorthite is consistent with the mineralogy of the wallrock units, which are calcic plutonic rocks or have been metamorphosed at amphibolite facies. Albite most likely formed during hydrothermal alteration at $\leq$300 °C associated with the brittle faulting, but the coexistence of albite and anorthite demonstrates that the wall rock mineralogy has not been completely replaced and is unlikely to be in equilibrium.

Ultracataclasite layers within the inner fault core and normal-sense shear fractures extending from the edge of the inner fault core truncate or offset the foliations, cataclasites, and pseudotachylytes in the outer fault core (Figs. 3c, 6 and 7). Ultracataclasite layers contain clasts of cataclasite from the outer fault core, but the reverse is not observed (Fig. 5a,b). Proportionally large amounts of laumontite and albite suggest a lower temperature of formation in the inner fault core than the outer fault core, as laumontite is unstable at temperatures above ~250 °C (Supplementary Material; Thompson, 1970). The ratio of albite to anorthite is much larger than for most of the outer fault core samples, reflecting the dominance of the alteration assemblage over preservation of detrital mineralogy in the gouge. As the inner fault core formed more recently and at lower temperature than the outer fault core, it could have formed during a phase of extensional reactivation documented to have occurred during the Miocene on nearby faults (*cf.* Axen and Fletcher, 1998). Unfortunately, the cumulative displacement of the inner fault core is unknown because of a lack of piercing points or other displacement indicators, and using length or thickness scaling relations to infer displacement may not be appropriate for reactivated faults (Shipton et al., 2006).

Layer m locally truncates all other deformation structures, including the inner-outer fault core contacts, indicating it was the last structure to form in the La Quinta Fault (Fig. 7a, b, c). The presence of smectite group clay in this layer indicates it formed at a lower temperature than the other ultracataclasite layers, which contain laumontite, chlorite, and illite, suggesting that layer m may

represent a fourth distinct phase of deformation and additional hydrothermal alteration of the mineral assemblage. Injection veins that extend from layer m into the hangingwall crosscut all other fault rocks (Fig. 7c). Ultracataclasite within the injections and layer m is homogeneous in composition and forms a single coherent unit. A slight foliation is seen within the layer at microscopic scale, but proportions of elements across the layer show no variation and no crosscutting relations within the layer are observed, suggesting shear deformation was distributed across the layer (Fig. 4d). Foliation in gouge or ultracataclasite material has been observed for experiments simulating creep, but also has been observed at seismic slip rates (Ujiie et al., 2013; French et al., 2014). The injection veins indicate that layer m was fluidized and overpressured, possibly due to coseismic shear (Otsuki et al., 2005; Lin, 2011; Rowe et al., 2012).

Layer m was identified in all five exposures that we studied and is present in exposures of the fault over 5 km away from the main study area (Fig. 1a), consistent with formation during a moderate-sized earthquake (Wells and Coppersmith, 1994). In some locations, layer m contains clasts of ultracataclasite but no other ultracataclasite layers are present. Layer m may therefore have entirely overprinted pre-existing ultracataclasite layers by wearing down all other layers, and/or have experienced significant granular flow during slip allowing mixing and long-distance transport of grains that obliterated earlier formed layers. We suggest that layer m represents at least one seismic slip event, but potentially many because the total displacement across the layer is unknown.

5. Geometric analysis

The geometries of the longest, most continuous traces of the inner-outer fault core edges; contacts between ultracataclasite layers within the inner fault core; and the upper and lower layer m contacts in the three largest exposures were quantified by calculating their Fourier power spectral density (Brown and Scholz, 1985; Power et al., 1988). Crosscutting relations within the inner fault core indicate that displacement was distributed across each layer with wear truncating previously formed layers at the margins of active layers. Each contact is therefore a cross section through what was once a principal slip surface. Similar analysis from cross sections through faults has been conducted previously (e.g. Griffith et al., 2010; Bistacchi et al., 2011). Each trace was extracted from the exposure maps, converted into a sequence of discretely sampled, uniformly spaced points, and detrended to remove bias.

The power spectral density (PSD) is a measure of the amplitudes of the spectral components of each contact trace. The trace geometries are consistent with a power law relationship between the PSD, $P(\lambda)$, and length scale, λ, of the form $P(\lambda) = C\lambda^{\beta}$, where C is a constant and β is the average slope in log-log space. The spectra of all contacts are comparable to previous studies that calculated the power spectra of fault surfaces from terrestrial laser scanner (TLS) data, with values of C (1 m) ranging from 10^{-4} to 10^{-6} and $2.5 < \beta < 3$ typical of slip-perpendicular values (Fig. 8) (e.g. Candela et al., 2012).

Layer m is the smoothest of the layers within the inner fault core as both the top and bottom edges of layer m have the smallest power of all contacts that we analyzed at all length scales (only the top of layer m is plotted, as it is representative of both) (Fig. 8a, Table 1). Layers c, d, f, g, h and l have greater power than layer m, so are rougher contacts (Note: layers f-g-h were analyzed as representative of the same event, because their relative ages were indistinguishable. See Supplementary Material for justification). Other than layer m, which is distinct, differences between spectra are extremely small, suggesting that roughness is not a function of relative layer age.

Because layers crosscut each other and clasts of older layers were broken off from layer edges, the primary shape of a layer when it was active may have been modified by later deformation, in which case layer m may be smoothest because it was not subsequently deformed (Fig. 6). To test this possibility, we categorized the traces of the contacts based on the combination of layers on either side of the contact to isolate the geometry that formed at different stages of the fault evolution. For example, the hangingwall outer fault-core (HWFC) trace was partitioned into the categories HWFC-a, HWFC-d, HWFC-k, HWFC-l, and HWFC-m. Each segment of data within a category represents the geometry of the slip surface when it was active, which was not modified by later deformation. The power spectra from each segment of data within a category were interpolated onto a single frequency vector and averaged over all contacts within that category to investigate the relationship between relative timing and contact roughness. As a consequence, some of the analyzed segments cover a relatively short range of length scales.

The hangingwall outer fault core contact with the layers of the inner fault core has a slightly different geometry depending on the layer adjacent to the contact (Fig. 8b). The smallest power and therefore smoothest contact is between the hangingwall outer fault core and layers a at short wavelengths and m at long wavelengths (Table 1). The differences between the spectra are small, but the roughest contacts are between layers d, k, l and the hangingwall outer fault core.

When the top contact of layer m is partitioned into segments based on the material above the contact, the results indicate a possible small dependence of the roughness on the adjacent material (Fig. 8c). The contact between m and the hangingwall outer fault core has the highest power at length scales less than ~10^{-1} m and a slope of 2.53 (Fig. 8b). Where layer m is in contact with layers d, k and l, it is marginally smoother (Table 1).

5.1. Method limitations

In comparison to recent works on fault geometry, our data set is limited as each trace that we analyzed is a single cross section through a given fault surface. Methods based on TLS point clouds of slickensides consider the entirety of a fault surface and average the power calculated at each frequency over thousands of traces, resulting in representative quantitative analyses (Sagy et al., 2007; Candela et al., 2012). Analysis of a single trace is sensitive to outliers in the overall geometry of a surface. However, the β values in our results are similar to those derived from surfaces measured in previous studies from TLS (Fig. 8) (Sagy et al., 2007), suggesting the contacts analyzed in cross section here are equivalent to one slip-perpendicular profile from fault surfaces analyzed using TLS and that the methodology that we employed is reasonable. Additionally, considering a single trace allows us to focus on the details of the geometry that record local geometric features, which may be averaged out by analyzing hundreds of traces. The value in utilizing these cross-sectional views is that they also allow comparison of the geometry of multiple surfaces or layers within a single fault core, which is impossible when considering one fault surface. Thus, we can consider fault evolution over time, which is not possible with a single slip surface that records multiple episodes of slip. In other words, our data speak to the 4D evolution of slip within a fault zone, allowing us to qualitatively but explicitly evaluate the relative impacts of intrinsic (e.g., mineralogy, grain size of previous cataclasite layers) and extrinsic (temperature and confining pressure) variations over time.

The cross-sectional views of the fault core are dependent on the trend of the cliff where the fault is exposed. Exposures trend 17° or less off fault strike, but variation in the exposure trend may cause

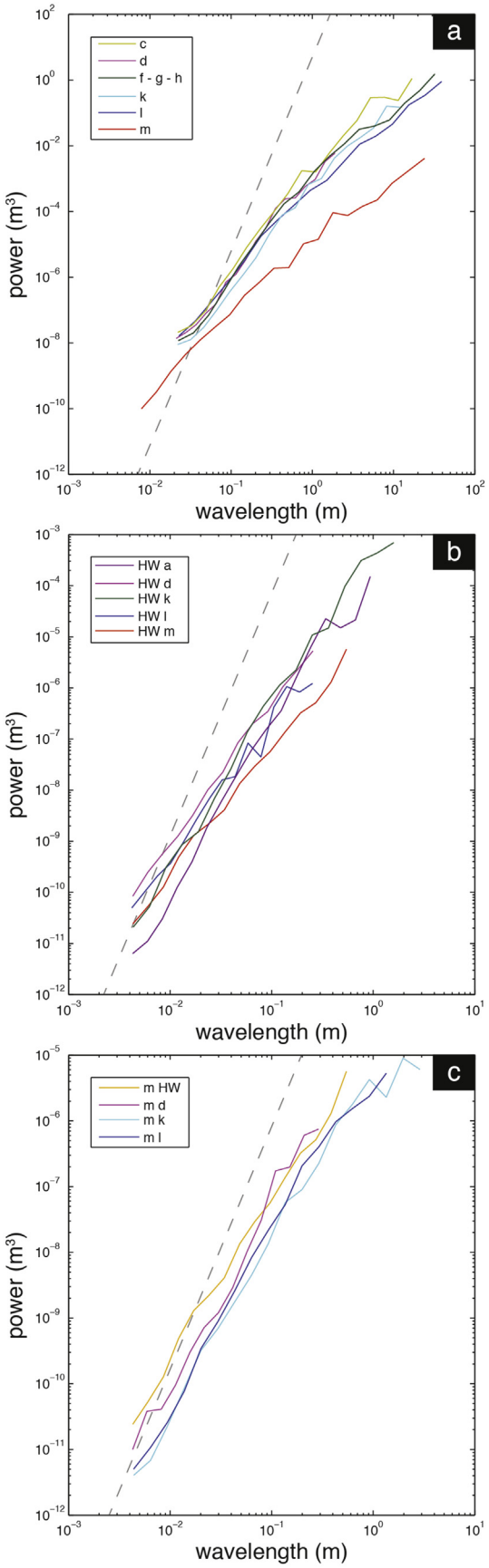

Fig. 8. PSD of contacts within the inner fault core. a: spectra of the complete contacts for layers within the inner fault core. b: PSD of the edges of layer m partitioned according to the material that layer m is in contact with. c: PSD of the hangingwall outer fault-core edge partitioned according to the layer adjacent to the it (see main text for description).

different estimates of roughness between exposures of the same contact (Lee and Bruhn, 1996; Candela et al., 2012). However, the Agisoft models were oriented perpendicular to dip (as indicated by slickenlines on exposed surfaces) at every exposure, so impacts of the differing exposure trend angles are minimized. A comparison of the hangingwall-outer fault core contact traces from each exposure shows that each has the same power and slope (Supplementary Material) indicating the models from different exposures are comparable.

PhotoscanPro creates slightly different models from the same set of input photos each time a model is created. We verified the precision of the maps by generating multiple models for one exposure from the same input photos and model parameters (Supplementary Material, section 3, Fig. S6). Test traces of the edge of the inner fault core were produced from each model. The PSD for the test traces were extremely similar at length scales of ~10^{-2} m and greater. Noise in the PSD at short length scales suggests small-scale (sub-cm) characteristics of the traces vary slightly between models. However, variability between the test traces was substantially less than the variability between different contacts suggesting the roughness measurements are reliable.

6. Discussion

Cross-sectional exposures of the La Quinta Fault provide a basis for assessing both the wear mechanisms that acted on the fault and the evolution of fault geometry constrained from crosscutting relations. Our analyses show that the youngest layer within the fault, which crosscuts all other structures, is the smoothest. However, the similarity in the roughness of all other layers preserved from different stages in the fault evolution indicates that the transition from rough to smooth was not pronounced prior to the formation of layer m. Below we discuss the processes that caused wear, and how they combined to change the shape of a fault surface with displacement.

6.1. Smoothing and re-roughening processes

Our observations document distinct wear processes on the La Quinta Fault at micrometer to meter scales that show the geometry of the fault is a function of a complex set of interrelated processes. At the smallest scale, rounded to sub-rounded grains as small as 1–10 μm were plucked from the contacts between layers (e.g. the outer fault core and layer m; Fig. 4e, f) and integrated into the actively deforming layer. Grain plucking caused the contacts between layers to re-roughen at the grain scale by creating embayments on the fault surface, rather than smoothing the contacts by shearing off portions of grains. Repeated removal of many grains could reduce the amplitudes of asperities larger than the grain scale, smoothing the layer contact at scales greater than the grain size. In exposure, centimeter-sized clasts are truncated by layer m, but in the samples that we analyzed in thin section, sub-centimeter sized clasts tend not to be cut by adjacent ultracataclasite layers (Fig. 7a). This relationship suggests that grain plucking is an important process for small (sub-centimeter) grains.

The formation of lenticular clasts within the inner fault core is also a smoothing and re-roughening process (Fig. 5). Based on the asymmetric geometry and long axes aligned with the layer edges, we interpret the lenses with a flat edge facing the protolith to represent asperities that were sheared off from a rough surface.

Table 1
Slopes, ß, of the PSD traces for contacts within the internal fault core, partitioned layer m contacts, and partitioned hangingwall – outer fault core contacts. Slopes for the internal fault core were calculated by taking an average of all contacts of each relative age. Slopes for the partitioned layer m and partitioned HWFC were calculated by taking an average of all contacts between specific internal fault core layers and layer m and specific internal fault core layers and the HWFC, respectively.

Internal fault core slopes (Fig. 8a)					
c	d	f-g-h	k	l	m
2.69	2.69	2.7	2.55	2.73	2.55
Partitioned layer m slopes (Fig. 8b)					
HWFC – m		d – m		k – m	l – m
2.53		2.64		2.74	2.84
Partitioned HWFC slopes (Fig. 8c)					
a – HWFC	d – HWFC	k – HWFC	l – HWFC	m – HWFC	
2.78	2.78	2.99	2.58	2.53	

Removing asperities is generally thought to be a process that results in a smoother surface (Archard, 1953). However, new fracture surfaces are relatively rough (Bouchaud et al., 1990). If the grain-scale plucking described above acted to smooth surfaces during displacement at wavelengths greater than the grain scale, any new fracture surface that formed where a lenticular asperity was sheared off may have been rougher than the surrounding surface. Lenticular clast formation may therefore have resulted in a fault surface that is smoother at scales greater than the lens dimension, but roughening at scales smaller than the lens dimension. The observation that many lenticular clasts have a minor axis length similar to the thickness of the layer in which they are contained indicates that the layer thickness limits the dimension of asperities that are sheared off.

Lenses where the flat edge is oriented away from the protolith formed as a slip zone splayed from the active slip zone layer into adjacent rock at a low angle, surrounding the lens (Fig. 7b). When this behavior occurred, the fault surface became rougher at the scales up to the dimension of the lenses, as a new fracture surface was locally integrated into the fault surface and the embayment around the lens roughened the surface. Similar formation of lenticular clasts within a fault core has been observed in multiple locations and at multiple scales (Chester et al., 2004; Cowan et al., 2003; Swanson, 2005). No clear field evidence suggests why the lenticular clasts formed in the La Quinta Fault, though one potential reason is exploitation of previously existing or syn-kinematic fractures in the outer fault core oriented at low angles to the fault. The formation of splays has also previously been linked to adhesion of a slip surface diverting slip onto a new surface (Swanson, 2005).

In some exposures, syn-kinematic displacement on subsidiary faults that branch from the inner-outer fault core contact and in some cases layer m, created local spikes in ultracataclasite thickness (similar to Watterson et al., 1998; Smith et al., 2007). Ultracataclasite filled the space created by displacement of the contact, and the slip zone in the inner fault core deformed to wrap around the irregular outer fault core block (Fig. 6). As the layer that thickened was syn-kinematic with the subsidiary fault, new asperities formed on the fault surface at decimeter to meter scale, the distances between subsidiary faults, although subsidiary faults are irregularly spaced. The subsidiary fault surface, rougher as it presumably experienced little wear, was integrated into the fault surface making the surface rougher at centimeter and decimeter scales.

These wear processes caused asperities to shear off and become clasts inside the active slip zone, which is interpreted to be a single ultracataclasite layer for any given stage in the fault history. The shape of the clasts may therefore record the shape of the fault surface when they were sheared off. However, rolling, fracturing and/or abrasion could have modified clasts during subsequent deformation within the inner fault core gouge, in which case their shapes would generally tend towards a more equidimensional aspect ratio (Monzawa and Otsuki, 2003). The most lenticular clasts therefore are the most likely to be a function of the shape of the fault surface when they were sheared off. A compilation of clast aspect ratios from all layers in the La Quinta Fault shows that larger clasts are more lenticular (Fig. 5c), whereas smaller clasts have a narrower range of aspect ratios, and are more equidimensional. The vast majority of clast aspect ratios we measured fall above an envelope of the form $L^{\zeta-1}$, where L is the clast long dimension (cm) and ζ is the Hurst exponent ($\zeta = (\beta - 1)/2$). Although grain plucking, lens incorporation by splays from the slip zone, and shear fracture propagation are different processes, the combined clast aspect ratios are described by a single scaling relation. Assuming the aspect ratio (H/L) is a proxy for the strain at failure, our data are consistent with the concept that the roughness of a fault surface records the scale dependent strength of the rock (Brodsky et al., 2016).

6.2. Roughness evolution

The combined effects of these smoothing and re-roughening processes should be evident in the power spectra evaluating the roughness of the slip surfaces. Crosscutting and truncation of older layers and clasts at the edge of each layer indicates that each layer acted as a principal slip zone at some stage during deformation. Field measurements have previously been used to show that fault surfaces change shape gradually with displacement (Brodsky et al., 2011), and lab experiments have also demonstrated that wear acts to change surface geometry (Wang and Scholz, 1994; Boneh et al., 2013; Lyakhovsky et al., 2014). These results suggest that, following initiation, some amount of smoothing of the slip surfaces at the edges of the layers should have occurred. Due to the lack of piercing points across and within the fault, we have no constraint on the displacement accommodated by each layer, or how many slip events, so the rate of smoothing with displacement cannot be evaluated. However, the outer fault-core contact represents the oldest contact analyzed, and where different layers are in contact with it, the effects of slip on those layers on the contact are preserved. Our results therefore isolate the roughness of layers at different stages of the fault activity within the inner fault core (Fig. 8b).

The analysis of the final shape of individual layers shows that the roughness of different layers is similar (Fig. 8b). This similarity could be explained by each layer initiating then accommodating one slip event. If each layer initiated with the same roughness, they may also have accommodated insufficient displacement to change shape sufficiently to be resolved with our methods. Alternatively, the lack of smoothing is consistent with the textural observations outlined in Section 6.1 that indicate a range of processes that served to both smooth and roughen the fault. These processes did affect the edge of each layer, and the accumulated effects of the wear processes should have changed the slip surface geometries, regardless of the amount of displacement. However, we have not been able to detect a corresponding change in the layer shape, which indicates the wear processes resulted in a minimal net change in roughness.

The PSD results emphasize that perhaps the most important process in the fault evolution was the formation of new slip surfaces. The inner fault core has up to 12 layers preserved in any given exposure, indicating new layer formation occurred many times

over the fault history, in contrast to geometrically simpler systems where the most recent slip zone accommodated the majority of displacement (Chester and Chester, 1998). Layer m has sharp, clearly defined edges and locally truncates adjacent, pre-existing layers and clasts within those layers at an angle rather than exploiting or localizing onto them. Similar characteristics are observed for other layers, and in some exposures, clasts of ultracataclasite that has no parent layer within the modern exposure indicate some layers were completely eliminated during deformation. We infer that the resulting angular discordance between layers developed when a new layer nucleated within an inner fault core containing pre-existing layer(s) of spatially variable thickness.

Layer m is notably different to the other layers in the inner fault core. It is the youngest component of the fault zone, is mineralogically distinct, and the contacts at the edges of layer m are smoother than the other layer edges we analyzed (Fig. 8a). This geometry indicates smoothing of the fault over the duration of deformation. However, layer m is the only layer that is not affected by subsequent activity on the fault, so the apparent smoothing shown in Fig. 8a may be due to re-roughening of the earlier-formed layers.

The roughness of the edges of layer m varies spatially depending on the ultracataclasite layer with which layer m has contact (Fig. 8c). Although differences in the power spectra of the portions of layer m edges partitioned according to the adjacent layer are relatively small, the results suggest that layer m is rougher when in contact with older layers. This correlation could be due to the grain-size distribution of the pre-existing layers. Our observations qualitatively indicate older layers are generally coarser grained with a wider range in grain size and larger proportions of clast compared to matrix. If these characteristics control the formation process, then they could result in spatially varying roughness. Alternatively, the variation in layer m roughness could result from faster wear rates where layer m was adjacent to finer grained layers. In either case, the results indicate that spatially variable roughness can be produced during deformation.

The mineral assemblage within layer m indicates substantial metasomatic changes accompanied formation and slip on the layer. Smectite clay and amorphous material were found only in layer m, and indicate formation at low temperature (<150 °C; Pytte and Reynolds, 1989). Clay-rich gouge is an important component of the mineralogy of the principal slip zone of the Punchbowl fault, where a positive feedback between comminution and alteration is inferred to have caused weakening and extreme localization (Chester et al., 2004). Similar processes may be key to the different geometry of layer m. We did not observe any direct evidence for dissolution in layer m, but the presence of clay must have altered the grain-scale deformation mechanisms and/or material properties to enable a smoother layer to form. For example, weak cohesion or the significantly smaller grain size of the ultracataclasite in layer m may account for its relative smoothness.

Overall, because the wear mechanisms that we described are likely to be important in many faults that deform by brittle deformation mechanisms, our observations of the La Quinta Fault highlight some processes that may be active in any fault. Specifically, the results demonstrate that the active slip surface within a fault zone can switch location within the fault core during deformation, and that any given surface within a fault core evolves with displacement slowly, if at all. Layer m, which was not subsequently modified by slip on the La Quinta Fault, may be representative of these processes, and shows that the initial shape of the new layer edges would be self-affine over the range wavelengths that we have analyzed. The net change in shape of a fault surface due to wear is gradual because wear processes both smooth and re-roughen a fault surface.

7. Conclusions

The La Quinta Fault in southern California is an exceptionally well-exposed structure with a multi-phase deformation history. At least thirteen ultracataclasite layers formed within the inner fault core during the most recent phase of brittle deformation. Based on truncation relations between adjacent layers, we interpret each layer to represent a slip zone, and the edges of the layers to be slip surfaces. Grain plucking, splaying of the slip zone into the adjacent wall rock, and syn-kinematic fracturing of asperities were the predominant wear mechanisms. Each mechanism acted to smooth and re-roughen the surfaces during deformation. Clast aspect ratios in the ultracataclasites indicate that the each process responded to the scale-dependent strength of the wall rocks. Formation of new layers occurred multiple times within the fault, which also resulted in changes to the slip zone composition and shape. Using cross-cutting relations, we defined the relative ages of the layers and measured the geometry of slip surfaces to reconstruct the evolution of geometry on a single fault. The power spectra of slip surfaces do not smooth substantially with increasing fault maturity, with the exception of the most recently formed layer, which may represent a distinct phase of deformation. Based on the power spectra, field observations, microstructural observations, and clast aspect-ratio scaling with length, we conclude that wear involves both smoothing and re-roughening processes. Within the La Quinta Fault, smoothing during deformation was predominantly caused by the nucleation of new smoother slip surfaces rather than wear of existing surfaces.

Acknowledgements

We thank Allan Muth and the UC Riverside Boyd Deep Canyon Nature Reserve for providing access and lodging for fieldwork. Thanks also to Anna Hissem for field support. Stereonets in Fig. 3 were produced using Stereonet 9; thanks to Rick Allmendinger for making the software publically available. Laurel Goodwin, an anonymous reviewer, and Editor Bill Dunne provided constructive reviews that greatly improved the paper. This work was funded in part by SCEC award 14074.

Appendix A. Supplementary data

Supplementary data related to this article can be found at http://dx.doi.org/10.1016/j.jsg.2016.09.004.

References

Aki, K., 1984. Asperities, barriers, characteristic earthquakes and strong motion prediction. J. Geophys. Res. 89, 5867–5872. http://dx.doi.org/10.1029/JB089iB07p05867.

Archard, J.F., 1953. Contact and rubbing of flat surfaces. J. Appl. Phys. 24 (8), 981–988.

Armstrong, R.L., Suppe, J., 1973. Potassium–argon geochronometry of Mesozoic igneous rocks in Nevada, Utah and southern California. Geol. Soc. Am. Bull. 84, 1375–1392. http://dx.doi.org/10.1130/0016-7606.

Axen, G.J., Fletcher, J.M., 1998. Late miocene-pleistocene extensional faulting, northern Gulf of California, Mexico and Salton trough, California. Int. Geol. Rev. 40, 217–244. http://dx.doi.org/10.1080/00206819809465207.

Bistacchi, A., Griffith, W.A., Smith, S.A.F., Di Toro, G., Jones, R., Nielsen, S., 2011. Fault roughness at seismogenic depths from LIDAR and photogrammetric analysis. Pure Appl. Geophys. 168, 2345–2363. http://dx.doi.org/10.1007/s00024-011-0301-7.

Boneh, Y., Sagy, A., Reches, Z., 2013. Frictional strength and wear-rate of carbonate faults during high-velocity, steady-state sliding. Earth Planet. Sci. Lett. 381, 127–137. http://dx.doi.org/10.1016/j.epsl.2013.08.050.

Boneh, Y., Chang, J.C., Lockner, D.A., Reches, Z., 2014. Evolution of wear and friction along experimental faults. Pure Appl. Geophys. 171 (11), 3125–3141. http://dx.doi.org/10.1007/s00024-014-0801-3.

Bouchaud, E., Lapasset, G., Planes, J., 1990. Fractal dimension of fractured surfaces: a universal value? Europhys. Lett. 13, 73. http://dx.doi.org/10.1209/0295-5075/13/

1/013.
Brodsky, E.E., Kanamori, H., 2001. Elastohydrodynamic lubrication of faults. J. Geophys. Res. 106, 16,357–16,374. http://dx.doi.org/10.1029/2001JB000430.
Brodsky, E.E., Gilchrist, J.J., Sagy, A., Collettini, C., 2011. Faults smooth gradually as a function of slip. Earth Planet. Sci. Lett. 302, 185–193. http://dx.doi.org/10.1016/j.epsl.2010.12.010.
Brodsky, E.E., Kirkpatrick, J.D., Candela, T., 2016. Constraints from fault roughness on the scale-dependent strength of rocks. Geology. http://dx.doi.org/10.1130/G37206.1.
Brown, S.R., Scholz, C.H., 1985. Closure of random elastic surfaces in contact. J. Geophys. Res. 90 (B7), 5531–5545. http://dx.doi.org/10.1029/JB090iB07p05531.
Candela, T., Renard, F., Klinger, Y., Mair, K., Schmittbuhl, J., Brodsky, E.E., 2012. Roughness of fault surfaces over nine decades of length scales. J. Geophys. Res. 117 (B08409) http://dx.doi.org/10.1029/2011JB009041.
Chester, F.M., Chester, J.S., 1998. Ultracataclasite structure and friction processes of the Punchbowl fault, San Andreas system, California. Tectonophysics 295, 199–221. http://dx.doi.org/10.1016/S0040-1951(98)00121-8.
Chester, F.M., Chester, J.S., 2000. Stress and deformation along wavy frictional faults. J. Geophys. Res. 105, 23,421–23,430. http://dx.doi.org/10.1029/2000JB900241.
Chester, F.M., Chester, J.S., Kirschner, D.L., Schulz, S.E., Evans, J.P., 2004. Structure of large displacement strike-slip faults. In: Karner, G.D., Taylor, B., Driscoll, N.W., Kohlstedt, D.L. (Eds.), Rheology and Deformation in the Lithosphere at Continental Margins. Columbia University Press, New York.
Cowan, D.S., Cladouhos, T.T., Morgan, J.K., 2003. Structural geology and kinematic history of rocks formed along low-angle faults, Death Valley, California. Geol. Soc. Am. Bull. 115, 1230–1248. http://dx.doi.org/10.1130/B25245.1.
Cowie, P.A., Scholz, C.H., 1992. Growth of faults by accumulation of seismic slip. J. Geophys. Res. 97 (B7), 11085–11095. http://dx.doi.org/10.1029/92JB00586.
Davidesko, G., Sagy, A., Hatzor, Y.H., 2014. Evolution of slip surface roughness through shear. Geophys. Res. Lett. 41, 1492–1498. http://dx.doi.org/10.1002/2013GL058913.
Dieterich, J.H., 1992. Earthquake nucleation on faults with rate- and state-dependent friction. Tectonophysics 211, 115–134. http://dx.doi.org/10.1016/0040-1951(92)90055-B.
Dieterich, J.H., Linker, M.F., 1992. Fault stability under conditions of variable normal stress. Geophys. Res. Lett. 19 (16), 1691–1694. http://dx.doi.org/10.1029/92GL01821.
Doblas, M., 1998. Slickenside kinematic indicators. Tectonophysics 295 (1–2), 187–197. http://dx.doi.org/10.1016/S0040-1951(98)00120-6.
Dokka, R.K., 1984. Fission-track geochronological evidence for late cretaceous mylonitization and early Paleocene uplift of the northeastern Peninsular ranges, California. Geophys. Res. Lett. 11, 46–49. http://dx.doi.org/10.1029/GL011i001p00046.
Dorsey, R.J., Housen, B.A., Janecke, S.U., Fanning, C.M., Spears, A.L.F., 2011. Stratigraphic record of basin development within the San Andreas Fault system: late cenozoic fish Creek- Vallecito basin, southern California. Geol. Soc. Am. Bull. 123, 771–793. http://dx.doi.org/10.1130/B30168.1.
Dunham, E.M., Belanger, D., Cong, L., Kozdon, J.E., 2011. Earthquake ruptures with strongly rate-weakening friction and off fault plasticity. Part 2: nonplanar faults. Bull. Seismol. Soc. Am. 101, 2308–2322. http://dx.doi.org/10.1785/0120100075.
Engelder, J.T., Scholz, C.H., 1976. The role of asperity indentation and ploughing in rock friction. 2: influence of relative hardness and normal load. Int. J. Rock Mech. Min. Sci. 13, 155–163.
Erskine, B.G., 1985. Mylonitic Deformation and Associated Low-angle Faulting in the Santa Rosa Mylonite Zone, Southern California. PhD thesis University of California, Berkeley, USA.
Erskine, B.G., 1986. Metamorphic and deformation history of the eastern Peninsular ranges mylonite zone: implications on tectonic reconstructions of southern California. Geol. Soc. Am. Abstr. Prog 18, 105.
French, M.E., Kitajima, H., Chester, J.S., Chester, F.M., Hirose, T., 2014. Displacement and dynamic weakening processes in smectite-rich gouge from the central deforming zone of the San Andreas fault. J. Geophys. Res. Solid Earth 119, 1777–1802. http://dx.doi.org/10.1002/2013JB010757.
Griffith, W.A., Nielsen, S., Di Toro, G., Smith, S.A.F., 2010. Rough faults, distributed weakening, and off-fault deformation. J. Geophys. Res. 115 (B08409) http://dx.doi.org/10.1029/2009JB006925.
Goodwin, L.B., Renne, P.R., 1991. Effects of progressive mylonitization on Ar retention in biotites from the Santa Rosa mylonite zone, California, and thermochronologic implications. Contrib. Mineral. Petrol. 108, 283–297. http://dx.doi.org/10.1007/BF00285937.
Janecke, S.U., Dorsey, R.J., Forand, D., Steely, A.N., Kirby, S.M., Lutz, A.T., Housen, B.A., Belgarde, B., Langenheim, V.E., Rittenour, T.M., 2010. High geologic slip rates since early pleistocene, initiation of the San Jacinto and San Felipe fault zones in the San Andreas fault system: southern California, USA. Special Paper Geol. Soc. Am. 475, 48. http://dx.doi.org/10.1130/2010.2475.
Johnson, K., Nissen, E., Saripalli, S., Arrowsmith, J.R., McGarey, P., Scharer, K., Williams, P., Blisniuk, K., 2014. Rapid mapping of ultrafine fault zone topography with structure from motion. Geosphere 10 (5). http://dx.doi.org/10.1130/GES01017.1.
Kirkpatrick, J.D., Brodsky, E.E., 2014. Slickenline orientations as a record of fault rock rheology. Earth Planet. Sci. Lett. 408, 24–34. http://dx.doi.org/10.1016/j.epsl.2014.09.040.
Lay, T., Kanamori, H., Ruff, L., 1982. The asperity model and the nature of large subduction zone earthquakes. Earthq. Predict. Res. 1, 3–71.
Lee, J.J., Bruhn, R.L., 1996. Structural anisotropy of normal fault surfaces. J. Struct. Geol. 18, 1043–1059. http://dx.doi.org/10.1016/0191–8141(96)00022–3.
Lin, A., 2011. Seismic slip recorded by fluidized ultracataclastic veins formed in a coseismic shear zone during the 2008 Mw 7.9 wenchuan earthquake. Geology 39 (6), 547–550. http://dx.doi.org/10.1130/G32065.1.
Linker, M.F., Dieterich, J.H., 1992. Effects of variable normal stress on rock friction: observations and constitutive equations. J. Geophys. Res. 97 (B4), 4923–4940. http://dx.doi.org/10.1029/92JB00017.
Ludington, S., Moring, B.C., Miller, R.J., Stone, P.A., Bookstrom, A.A., Bedford, D.R., Evans, J.G., Haxel, G.A., Nutt, C.J., Flyn, K.S., Hopkins, M.J., 2005. Preliminary Integrated Geologic Map Databases for the United States - Western States: California, Nevada, Arizona, Washington, Oregon, Idaho, and Utah. USGS. Open-File Report 2005–1305.
Lyakhovsky, V., Sagy, A., Boneh, Y., Reches, Z., 2014. Fault wear by damage evolution during steady-state slip. Pure Appl. Geophys. 1 (15) http://dx.doi.org/10.1007/s00024-014-0787-x.
Matti, J.C., Cox, B.F., Powell, R.E., Oliver, H.W., 1983. Mineral resource Potential of the Cactus Spring Roadless Area, Riverside County, California. USGS. Report accompanying Map 1650-A.
Matti, J.C., Morton, D.M., Cox, B.F., Landis, G.P., Langenheim, V.E., Premo, W.R., Kistler, R., Budahn, J.R., 2006. fault-bounded late neogene sedimentary deposits in the Santa Rosa mountains, southern CA: constraints on the evolution of the San Jacinto fault. Eos, Trans. Am. Geophys. Union 87 (52) (Fall Meeting Supplement, Abstract).
Monzawa, N., Otsuki, K., 2003. Comminution and fluidization of granular fault materials: implications for fault slip behavior. Tectonophysics 376, 127–143. http://dx.doi.org/10.1016/S0040-1951(03)00133-1.
Morton, D.M., Miller, F.K., Kistler, R.W., Premo, W.R., Lee, C.-T.A., Langenheim, V.E., Wooden, J.L., Snee, L.W., Clausen, B.L., Cossette, P., 2014. Framework and petrogenesis of the northern Peninsular ranges batholith, southern California. Geol. Soc. Am. Mem. 211, 61–143. http://dx.doi.org/10.1130/2014.1211(03).
Okubo, P.G., Dieterich, J.H., 1984. Effects of physical fault properties on frictional instabilities produced on simulated faults. J. Geophys. Res. 89 http://dx.doi.org/10.1029/JB089iB07p05817.
Otsuki, K., Uduki, T., Monzawa, N., Tanaka, H., 2005. Clayey injection veins and pseudotachylyte from two boreholes penetrating the Chelungpu fault, Taiwan: their implications for the contrastive seismic slip behaviors during the 1999 Chi-Chi earthquake. Isl. Arc 14 (1), 22–36. http://dx.doi.org/10.1111/j.14401738.2004.00455.x.
Parsons, T., 2008. Persistent earthquake clusters and gaps from slip on irregular faults. Nat. Geosci. 1, 59–63. http://dx.doi.org/10.1038/ngeo.2007.36.
Power, W.L., Tullis, T.E., Brown, S.R., Boitnott, G.N., Scholz, C.H., 1987. Roughness of natural fault surfaces. Geophys. Res. Lett. 14, 29–32.
Power, W.L., Tullis, T.E., Weeks, J.D., 1988. Roughness and wear during brittle faulting. J. Geophys. Res. 93 (B12), 15268–15278. http://dx.doi.org/10.1029/JB093iB12p15268.
Pytte, A.M., Reynolds, R.C., 1989. The thermal transformation of smectite to illite. In: Naeser, N.D., McCulloh, T.H. (Eds.), Thermal history of Sedimentary Basins: Methods and Case Histories. Springer-Verlag, New York, pp. 33–40.
Rasband, W.S., 1997. ImageJ. U. S. National Institutes of Health, Bethesda, Maryland, USA, 2014. http://imagej.nih.gov/ij.
Renard, F., Voisin, C., Marsan, D., Schmittbuhl, J., 2006. High resolution 3D laser scanner measurements of a strike-slip fault quantify its morphological anisotropy at all scales. Geophys. Res. Lett. 33 (L04305) http://dx.doi.org/10.1029/2005GL025038.
Rowe, C.R., Kirkpatrick, J.D., Brodsky, E.E., 2012. Fault rock injections record paleoearthquakes. Earth Planet. Sci. Lett. 335–336, 154–166. http://dx.doi.org/10.1016/j.epsl.2012.04.015.
Sagy, A., Brodsky, E.E., Axen, G.J., 2007. Evolution of fault-surface roughness with slip. Geology 35, 283–286. http://dx.doi.org/10.1130/G23235A.1.
Scholz, C.H., 1987. Wear and gouge formation in brittle faulting. Geology 15 (6), 493–495.
Sharp, R.V., 1967. San Jacinto fault zone of the peninsular ranges of southern California. Geol. Soc. Am. Bull. 78, 705–729.
Sharp, R.V., 1979. Some characteristics of the eastern peninsular ranges mylonite zone. Open File Report. In: Proceedings of the Conference on Analysis of Actual Fault Zones in Bedrock, vol. 79, pp. 258–267.
Shi, Z., Day, S.M., 2013. Rupture dynamics and ground motion from 3D rough-fault simulations. J. Geophys. Res. 118, 1122–1141. http://dx.doi.org/10.1002/jgrb.50094.
Shipton, Z.K., Soden, A.M., Kirkpatrick, J.D., Bright, A.M., Lunn, R.J., 2006. How thick is a fault? Fault displacement–thickness scaling revisited. In: Abercrombie, R., McGarr, A., di Toro, G., Kanamori, H. (Eds.), Earthquakes: Radiated Energy and the Physics of Faulting, Geophysical Monograph, vol. 170. American Geophysical Union, pp. 193–198.
Sibson, R.H., 1986. Brecciation processes in fault zones: inferences from earthquake rupturing. Pure Appl. Geophys. 124 (1–2), 159–175. http://dx.doi.org/10.1007/BF00875724.
Smith, S.A.F., Holdsworth, R.E., Collettini, C., Imber, J., 2007. Using footwall structures to constrain the evolution of low-angle normal faults. J. Geol. Soc. 164 (6), 1187–1191.
Swanson, M.T., 2005. Geometry and kinematics of adhesive wear in brittle strike-slip fault zones. J. Struct. Geol. 27, 871–887. http://dx.doi.org/10.1016/j.jsg.2004.11.009.
Thompson, A.B., 1970. Laumontite equilibria and the zeolite facies. Am. J. Sci. 269,

267–275.
Todd, V.R., Erskine, B.G., Morton, D.M., 1988. Metamorphic and tectonic evolution of the northern Peninsular ranges batholith southern California. Rubey. In: Ernst, W.G. (Ed.), Metamorphic and Crustal Evolution of the Western U.S, vol. VII. Prentice-Hall, pp. 894–937.
Ujiie, K., Tanaka, H., Saito, T., Tsutsumi, A., Mori, J.J., Kameda, J., Brodsky, E.E., Chester, F.M., Eguchi, N., Toczko, S., Expedition 343 and 343T Scientists, 2013. Low coseismic shear stress on the Tohoku-Oki megathrust determined from laboratory experiments. Science 342, 1211–1214. http://dx.doi.org/10.1126/science.1243485.
Verhoeven, G., 2011. Taking computer vision aloft -archaeological three-dimensional reconstructions from aerial photographs with photoscan. Archaeol. Prospect. 18, 67–73. http://dx.doi.org/10.1002/arp.399.
Wang, W., Scholz, C.H., 1994. Wear processes during frictional sliding of rock: a theoretical and experimental study. J. Geophys. Res. 99 (B4), 6789–6799. http://dx.doi.org/10.1029/93JB02875.
Watterson, J., Childs, C., Walsh, J.J., 1998. Widening of fault zones by erosion of asperities formed by bed-parallel slip. Geology 26, 71–74.
Wells, D.L., Coppersmith, K.J., 1994. New empirical relationships among magnitude, rupture length, rupture width, rupture area, and surface displacement. Bull. Seismol. Soc. Am. 84, 974–1002.
Wenk, H.R., Johnson, L.R., Ratschbacher, L., 2000. Pseudotachylytes in the eastern peninsular ranges of California. Tectonophysics 321, 253–277. http://dx.doi.org/10.1016/S0040-1951(00)00064-0.
White, B.C., 2006. Structural geology of the eastern central Santa Rosa Mountain, RiversideCounty. Masters thesis, p. 48.
Wilson, J.E., Chester, J.S., Chester, F.M., 2003. Microfracture analysis of fault growth and wear processes, Punchbowl Fault, San Andreas system, California. J. Struct. Geol. 25, 1855–1873.